KLOE Note 134/95
January 1995

Module Zero,
Analysis of the 1994 Test Beam at PSI

Sabine Wölfle

Laboratori Nazionali di Frascati, I-00044 Frascati, Italy.

1 Introduction

The first full scale module "Module Zero" for the KLOE electromagnetic calorimeter was taken to the Paul–Scherrer–Institut PSI in July 1994 to be tested with electron, muon and pion beams in a momentum range of 100 – 450 MeV/c. Data were collected during more than 300 runs for particles hitting the calorimeter module at different y– and z–positions and under different incidence angles θ and φ.
This note gives a comprehensive report on the data analysis and the results both on energy response and resolution and on timing properties. We restrict ourselves to the data taken with commercial CAMAC ADCs and TDCs[1].

2 Experimental Setup

A module of the *barrel* part of the KLOE electromagnetic calorimeter has a length of 4.17 m and a trapezoidal cross section as displayed in figure 1 with a thickness of 23 cm. We will use the local coordinate system of a *barrel* module as defined in [And 94], where the origin lies in the centre of the calorimeter surface facing the beam. The beam is going in x–direction, the z–axis runs in fibre direction and the y–coordinate has been chosen to form a righthanded coordinate system.
The first half of the module thickness was assembled using Kuraray fibres, the back part was built with Pol.Hi.Tech fibres.
The readout is organized in five planes (in x–direction) and twelve columns (in y–direction) with a cell granularity of 4.4×4.4 cm^2 in the first plane up to 5.4×4.8 cm^2 in the last plane.
For the first time the mesh phototubes Hamamatsu R5946 – the final choice for the KLOE experiment – were used. Their quantum efficiency is 45 % less than that for linear focussed PMs, as reported in [Kee 94].
The readout chain after the PMs consists of preamplifiers ($\times 5$) directly mounted to the PM base and active splitters which distribute the analog signal to the ADCs and to constant fraction discriminators. The discriminated signal served as a stop for the TDCs, whereas

[1] A part of the datataking was dedicated to test the KLOE design VME ADCs and TDCs.

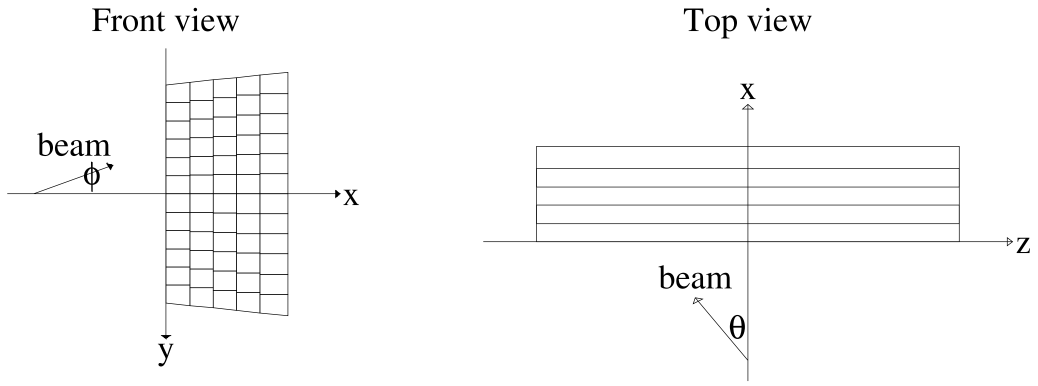

Figure 1: Definition of coordinate system and angles.

the start was provided by the trigger.
The coincidence of three scintillator counters was acting as the trigger signal, two of them formed a cross right in front of the calorimeter, thus defining a beam spot of $1.0 \times 1.0\,\mathrm{cm}^2$. The third one was located at a distance of (354 ± 1) cm in upstream direction to enable time of flight measurements necessary for particle identification.
Due to a technical problem the module was tilted against the vertical by $\varphi = 5°$.

3 Data Analysis

For the first time the complete test beam analysis including calibration was performed in the environment provided by Analysis_Control [CDF 93]. The list mode raw data were read by the input module and then organized in YBOS banks which in turn could be easily accessed by other modules. All calibration data were stored in HEPDB databases [Pel 94] and can easily be accessed by dedicated subroutines (for a more technical description see [Wöl 95]).

4 Calibration

4.1 ADC Pedestals

To facilitate the determination of the ADC pedestals so–called pedestal events were triggered randomly during the runs with a time unit. A filter module could select these events easily by requiring that the TDCs of the trigger counters had seen no signal, i.e. were all in overflow. The efficiency of this method is shown in figure 2. The pedestal values were taken as the mean value of the distributions and had a rms of typically less than 1 channel. They were determined on a run by run basis for each readout channel and stored in the run condition database.

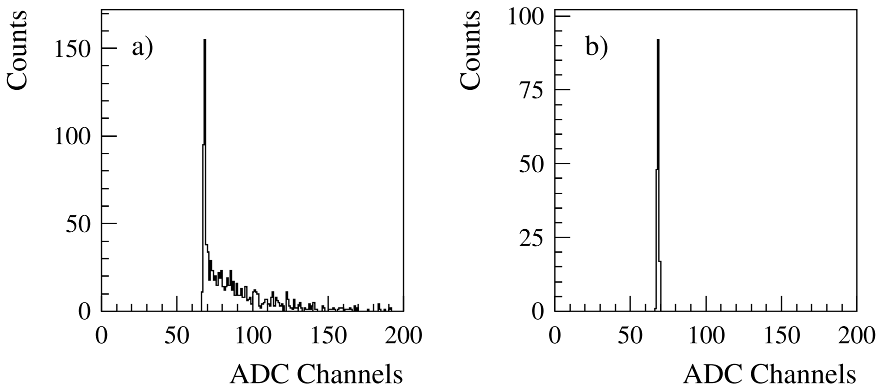

Figure 2: ADC spectrum for cell 91: a) before and b) after pedestal filter

4.2 Energy Calibration

Before being mounted on the module all PMs were tested at Frascati to measure their gain dependence on the high voltage. Using these results the high voltage values were chosen to ensure a gain of $5 \cdot 10^6$, typically they were around 1800 – 2000 V. This procedure was only accurate on a 10% level, moreover some tubes would have required a voltage value

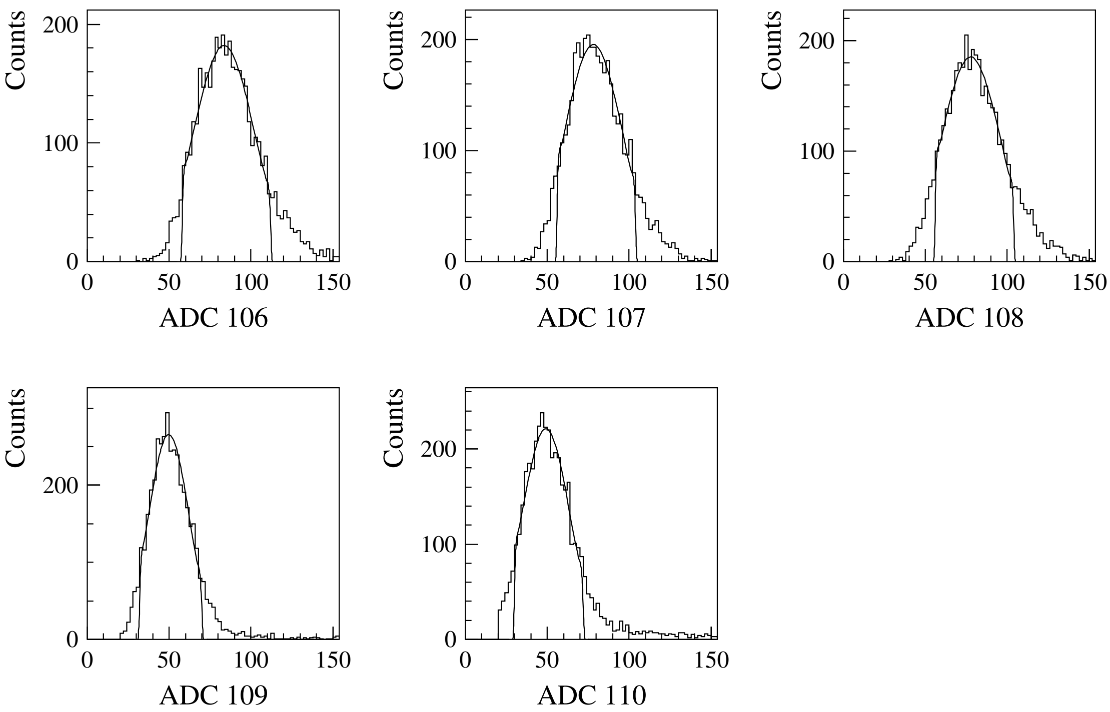

Figure 3: ADC spectra and fits for m.i.p.s in column 10, side B

larger than allowed by the HV system.
Thus a more precise energy calibration was performed using a π^- beam at 450 MeV/c scanning all detector columns. Monte Carlo simulations have shown that 450 MeV/c pions can be considered as minimum ionizing particles (m.i.p.s) even after having traversed the complete thickness of the calorimeter module [Gio 94].
Only those events were considered for calibration where the pion had passed the complete column thus avoiding events where the pion had stopped or made a nuclear (e.g. charge exchange) reaction. A large amount of data was rejected because the pion entered the neighbour column due to the $\varphi = 5°$ tilt of the module.
The first pass on the events expressed all energy cuts in ADC channels (after pedestal subtraction): less than 20 channels on the column to be calibrated, more than 20 channels on the two neighbour columns. $5 - 10\%$ of all events passed these cuts, the energy distribution of each ADC was fitted with a Gaussian in a region where the signal was higher than 40 % of the peak value. The fits for column 10, side B are shown in figure 3.
The mean value of the Gaussian function was taken as the calibration constant. To keep the energy units from this test run comparable with those from older test beams, we defined 1 mip as the visible energy deposited by a m.i.p. in 3.5 cm of calorimeter material[2]. Thus we had to apply a geometrical correction factor of $4.4/3.5 = 1.26$ for the first four planes and $5.4/3.5 = 1.54$ for the last plane.
In a second step the whole procedure was repeated, but now all cuts were expressed in mip values to ensure the same selection criteria for each cell because the difference of the calibration constants was as large as a factor of 2.

4.3 Time Walk Corrections

Although we used constant fraction discriminators there still is some dependence left of the trigger timing on the signal amplitude. We parametrized the walk curves using the following formula:

$$TDC(ADC) = a + \frac{b}{\sqrt{ADC}} ,$$

where TDC and ADC denote TDC and ADC channels.
They were obtained for each run, each readout cell[3] and each particle type. The reason for the different walk curves for different particles within the same run is not yet fully understood and requires further investigation. One explanation might be the different signal shape of a showering electron compared to a straight throughgoing pion.
For different runs belonging to the same z–scan we used the walk parameters obtained form the run at $z = 0$. This can be justified by figure 5 where walk parameters b for all z–positions were determined individually and are plotted for various readout cells. The maximum discrepancy from the $z = 0$ value is 300 ps at 1 mip.

4.4 Time Offsets T_0

The time offsets were obtained by fitting a Gaussian function to the already walk–corrected time distributions. In accordance with the walk corrections time offsets were determined

[2]Earlier prototypes had a granularity of 3.5×3.5 cm^2.
[3]Only cells within ± 2 columns around the one hit by the beam were taken into account; the others were lacking statistics.

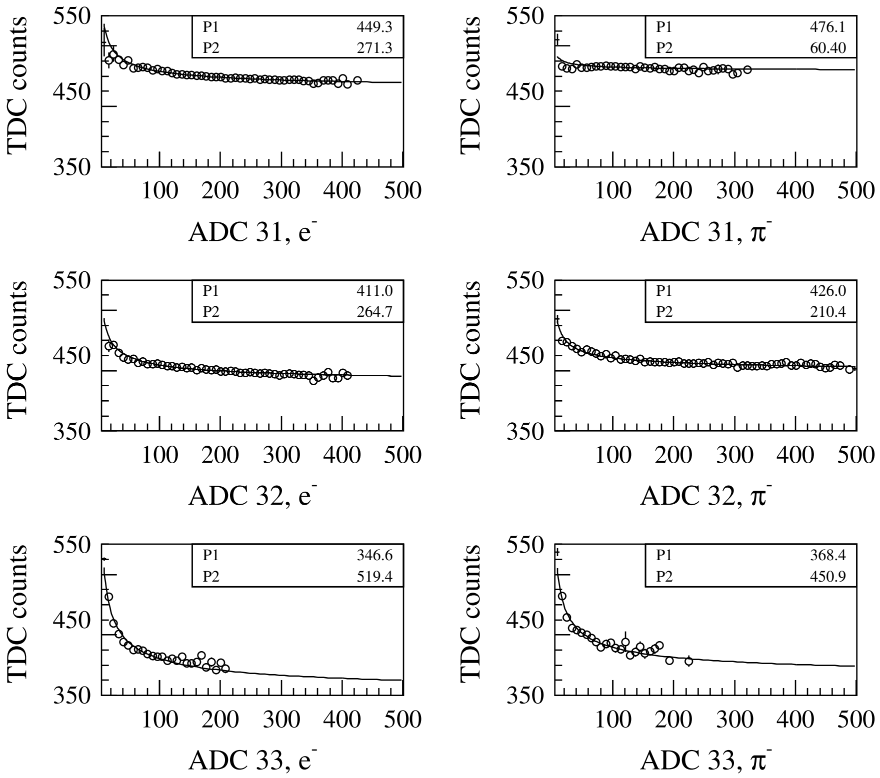

Figure 4: Walk corrections for a 250 MeV/c run, note the differences between electrons and pions.

under exactly the same circumstances, i.e. for each run, each readout cell and each particle type. Different particle types have different time of flights and thus different offsets. In order not to lose the z–information the values taken from the $z = 0$ runs were applied to all runs originating from the same z–scan.

4.5 TDC Calibration

Two different types of TDCs were employed in the test beam. Side A was equipped with Philipps TDCs, side B with CAEN TDCs. The nominal gain for both of them was 25 ns/chan.

One attempt of calibrating the TDCs was done during the test beam itself by comparing the time offsets of two runs, one of which had an additional offset of 10 ns. The disadvantage of this method is the choice of just a small range, moreover the TDC values for side A were in the non–linear region.

After the test beam all TDCs were calibrated over their complete range [Mur 94], but unfortunately the correspondence between readout cell and TDC channel was not written down. The results of this "post–beam" calibration is displayed in figure 6. It can be seen

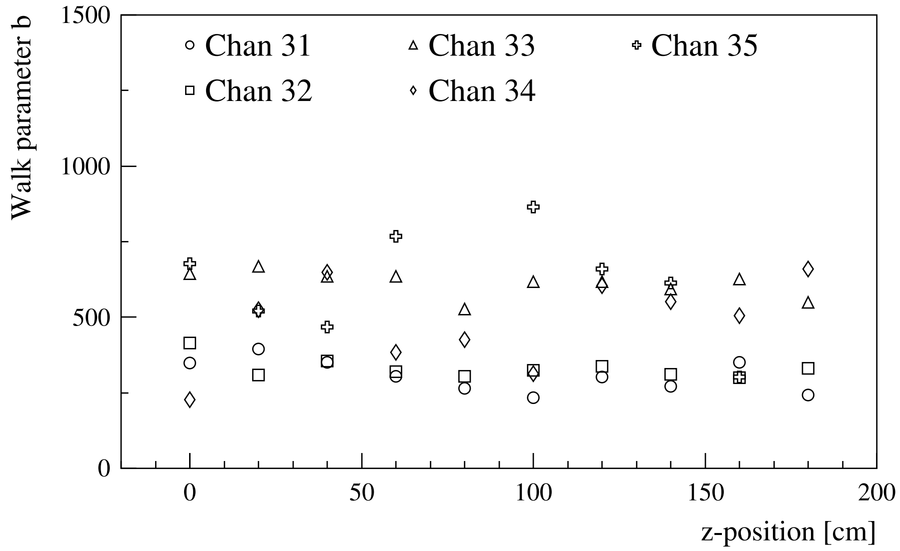

Figure 5: Walk correction parameters b for different z–positions.

clearly that the Philips TDCs behave very uniformly and their gain g could therefore be parametrized as a function of the TDC channel t as follows:

$$g(t) = \begin{cases} 51.15 - 0.154\,t + 2.2 \cdot 10^{-4}\,t^2, & t < 431 \text{ chan} \\ 28.85 - 4.38 \cdot 10^{-4}\,t, & t \geq 431 \text{ chan} \end{cases} \tag{1}$$

Using this calibration and the assumption that light propagation velocities v_{eff} are the same for A and B side one can measure the v_{eff} on side A (i.e. for the Philips TDC) and deduce from these values an "overall" TDC gain for each individual CAEN TDC of side B, cf. section 5.3 for the method of determining v_{eff}.

To compare the two sets of TDC calibration data the time resolution values for three different e^- runs were calculated, see table 1. As there was no improvement found when substituting the nominal TDC gain of 25 ps/chan by a special calibration all the following analyses were done with this value.

Table 1: Time resolution values (in ps) with different TDC calibration data

Method	125 MeV, col 7	250 MeV, col 7	250 MeV, col 6
Nominal gain	238 ± 2	197 ± 3	194 ± 3
10 ns delay	242 ± 2	202 ± 3	142 ± 2
"post–beam"	239 ± 2	197 ± 3	192 ± 3

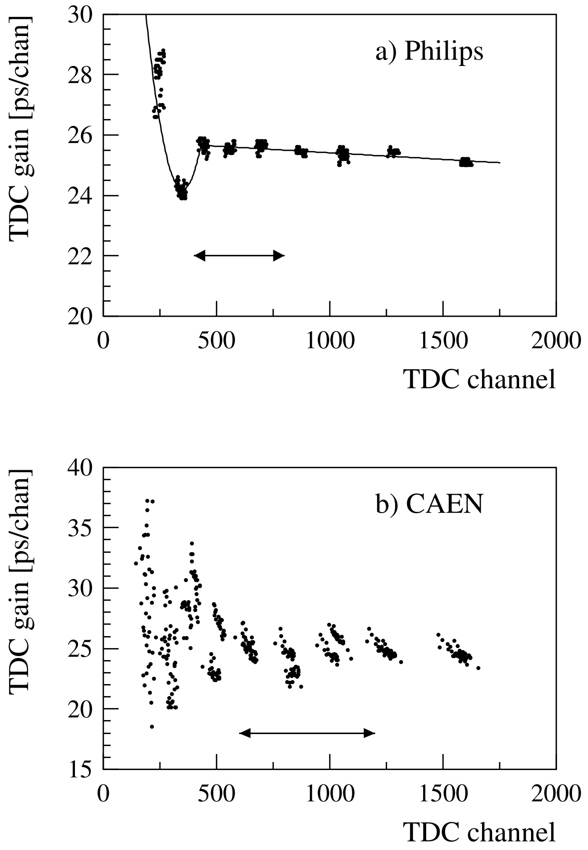

Figure 6: Results from "post–beam" TDC calibration, all channels and delays combined in one plot. The arrays indicate the region where the TDCs were operated.
a) Philips TDC with parametrization, b) CAEN TDC

5 Fibre Characteristics

5.1 Light Output

The light output of the different fibres in photoelectrons per mip (pe/mip) can be calculated with the knowledge of the gains of the phototubes g_{PM}, the gain of the ADCs g_{ADC} and the ADC response for a mip A_{mip} for each readout cell:

$$N_{pe} = \frac{A_{mip} \cdot g_{ADC}}{g_{PM}}$$

with: $g_{ADC} = 0.25$ pC/chan $= 1.56 \cdot 10^6$ e/chan
$g_{PM} = 5 \cdot 10^6$

The results for the single cells were averaged only over the planes to take into account the different fibres in the different fibre types. Results are shown in table 2.

Table 2: Fibre characteristics as a function of plane number

Plane	N_{pe}	λ [cm]	v_{eff} [cm/ns]
1	26.1	338	17.1
2	26.5	361	17.1
3	22.7	315	17.3
4	16.9	249	17.4
5	16.9	228	17.5

5.2 Attenuation Length

The attenuation length of the fibres was determined using m.i.p. runs from a scan in z–direction. Single side energy data from ten different z–positions (0 – 180 cm) were used. To cover also the negative z–range up to -180 cm the energy values from the opposite side were used. Figure 7 shows the peak value of the single energy distribution plotted versus the z–position for column 6. The curve was fitted with one exponential starting at least 50 cm from the readout end to avoid contributions from the short attenuation length of the cladding:

$$E(z) = E(0) \cdot e^{-z/\lambda} \ .$$

The values for λ are reported in table 2, the error from the fit lies in the order of 1%. The two fibre types can be clearly distinguished by their different attenuation lengths.

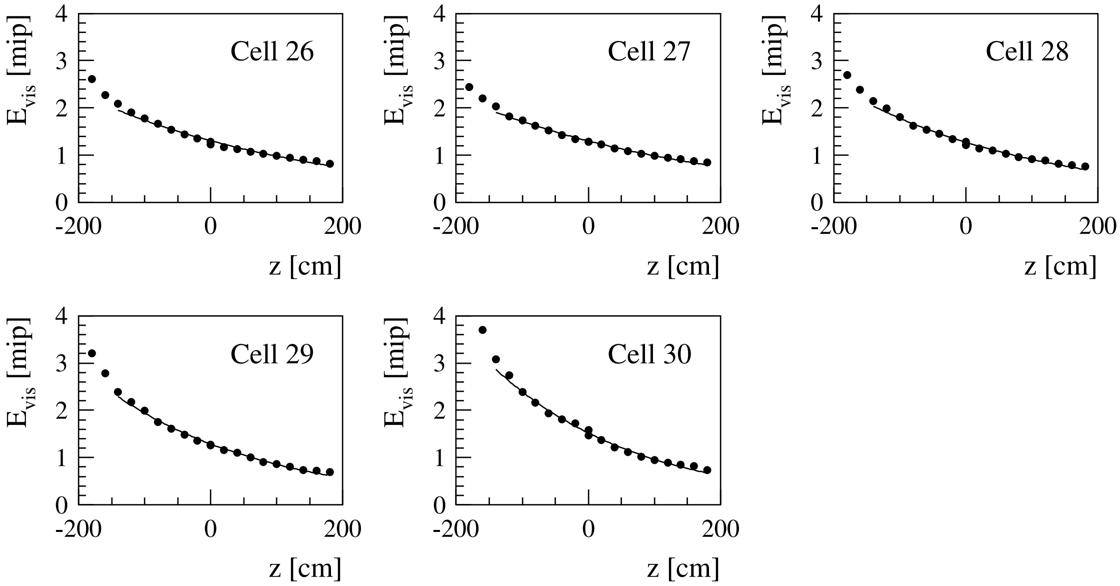

Figure 7: Attenuation length curves for column 6.

5.3 Light Propagation Velocities

The same m.i.p. runs used for the determination of the attenuation length were also employed to evaluate the effective light propagation velocity of the scintillation light in the fibres. Because of the problems with the TDC calibration we restricted ourselves to look at the TDC values from side A instrumented with the Philips TDCs, using the parametrization (1) for the TDC calibration. In figure 8 we have plotted the time walk and T_0 corrected TDC values (taking the mean value of the single distribution) versus the z–position and fitted them with a straight line. The slope of the straight line gives us the inverse light propagation velocity:

$$T(z) - T_0 = z \cdot {v_{eff}}^{-1} \ .$$

Results are presented in table 2. There seems to be a fibre dependence in the order of 2% that could be ascribed to different refraction indeces.

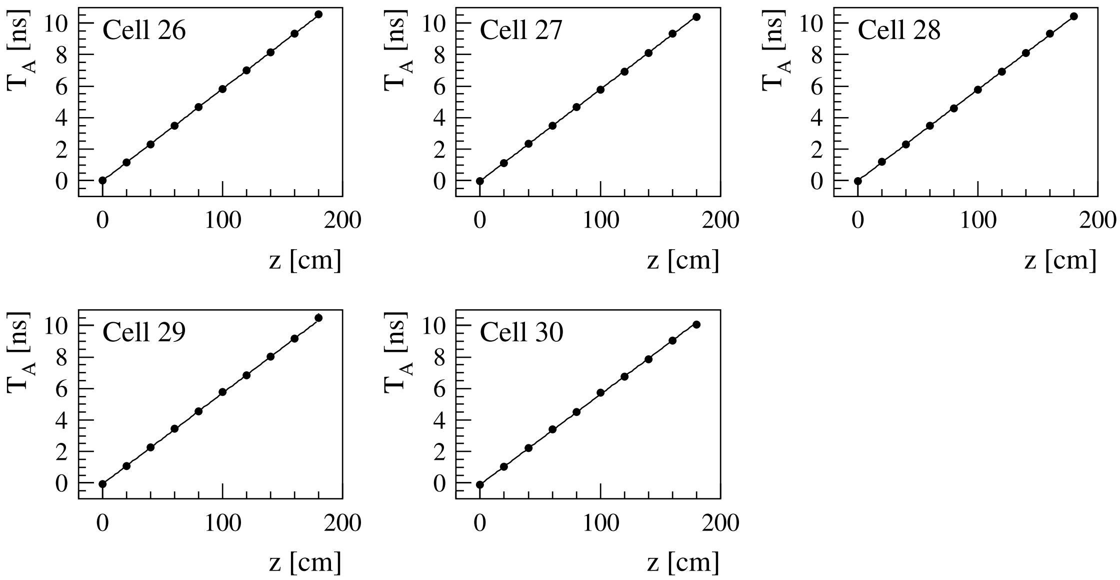

Figure 8: TDC times vs. z–position for side A, the slope of the straight line gives ${v_{eff}}^{-1}$.

6 Energy Response and Resolution

For all energy analyses only those cells were taken into account where both A and B side energies E_A and E_B were above 0.05 mip. The single side energies of these n cells were added up to yield the visible energy of the event

$$E_{vis} = \sum_{i=1}^{n} \frac{1}{2} \left(E_{A,i} + E_{B,i} \right) \ .$$

6.1 Energy loss of beam in front

The material the beam had to pass in front of the calorimeter consisted of the trigger counters plus a strawtubes detector, in total equivalent to 2.67 cm of polystyrene. Thus the energy loss for electrons was

$$E_{loss} = 2.67\,\mathrm{cm} \cdot 2.01\,\mathrm{MeV/cm} = 5.37\,\mathrm{MeV}\ .$$

In the energy range of the test beam muon and pions are not m.i.p.s, so their energy loss before entering the calorimeter is a function of energy and had to be simulated. It ranges between 6 and 10 MeV and was correctly subtracted from the beam energy to give the kinetic energy of the particles. .

6.2 Energy Response and Sampling Fraction

Electrons

The visible energy as a function of the kinetic energy of the beam is plotted for all incidence angles in figure 9. The superimposed straight line is a linear fit for the data at $\varphi = 0°$ and

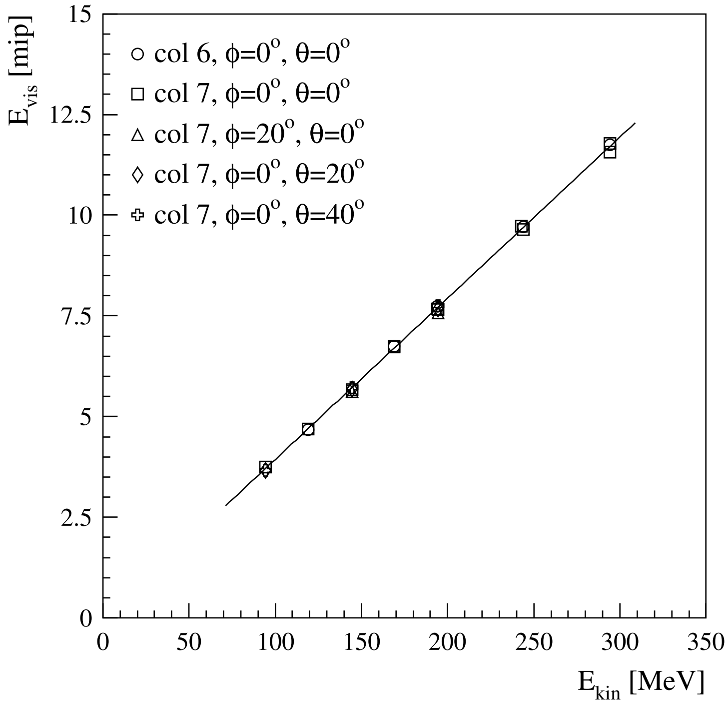

Figure 9: Energy response for electrons, fit is for normal incidence only.

$\theta = 0°$ only, but a look at table 3 confirms that the values for all angles do agree within the errors. The slope is

$$s_{em} = (40.0 \pm 0.2)\ \mathrm{mip/GeV}\ ,$$

offsets are compatible with zero.
With a value of 3.24 MeV per mip from Monte Carlo simulations we can give the sampling

fraction for electromagnetic showers as follows:

$$f_{em} = \frac{E_{vis}}{E_{kin}} = s_{em} \cdot 3.24 \, \frac{\text{MeV}}{\text{mip}} = (13.0 \pm 0.1) \,\% \ .$$

Table 3: Energy response for electrons for different incidence angles

φ	θ	s_{em} [mip/GeV]	offset [mip]
0°	0°	40.0 ± 0.2	-0.069 ± 0.028
20°	0°	39.0 ± 1.1	-0.019 ± 0.186
0°	20°	40.2 ± 0.8	-0.141 ± 0.104
0°	40°	40.0 ± 0.2	-0.195 ± 0.106

Muons

In figure 10 the energy response for muons is plotted as a function of their kinetic energy. The points at $E_{kin} \approx 160$ MeV were not taken into account when fitting because at these

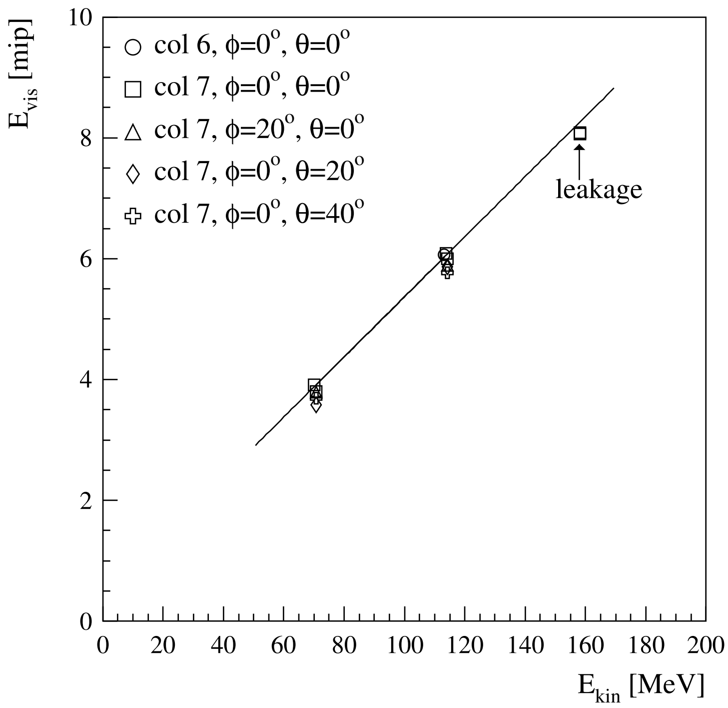

Figure 10: Energy response for muons, fit is for normal incidence only.

energies the muons were already leaking outside the calorimeter. Again the superimposed straight line is for $0°$ values only and has a slope of

$$s_\mu = (49.8 \pm 1.2)\ \mathrm{mip/GeV}\ ,$$

which in turn gives a sampling fraction of

$$f_\mu = s_\mu \cdot 3.24\,\frac{\mathrm{MeV}}{\mathrm{mip}} = (16.1 \pm 0.4)\,\%\ .$$

Results for different incidence angles can be found in table 4. The agreement is not as good as in the electrons' case but we have to consider that the "fit" was done with two points only for non–zero incidence angles. This is probably also the reason why the offsets differ significantly from zero.
The ratio between the energy response for electrons and muons stopping in the calorimeter at $0°$ incidence is

$$\frac{f_{em}}{f_\mu} = 0.803 \pm 0.09\ .$$

Table 4: Energy response for muons at different incidence angles

φ	θ	s_μ [mip/GeV]	offset [mip]
$0°$	$0°$	49.8 ± 1.2	0.394 ± 0.108
$20°$	$0°$	48.2 ± 2.6	0.381 ± 0.233
$0°$	$20°$	52.5 ± 2.1	-0.135 ± 0.192
$0°$	$40°$	47.5 ± 2.4	0.334 ± 0.216

Pions

Pions not only lose their kinetic energy by ionization but can also undergo nuclear reactions. This contribution can be seen as the large tails down to low energies in figure 11. To determine the energy response of the pions only a small region around the peak was fitted with a Gaussian function with the peak values plotted in figure 12. Again the point at $E_{kin} \approx 180$ MeV was ignored for the linear fit because of back leakage. For $0°$ incidence angles we get for the slope

$$s_\pi = (48.9 \pm 0.8)\ \mathrm{mip/GeV}$$

and hence a sampling fraction of

$$f_\pi = s_\pi \cdot 3.24\,\frac{\mathrm{MeV}}{\mathrm{mip}} = (15.8 \pm 0.3)\,\%\ .$$

Within the errors the values for the sampling fractions of muons and pions stopping in the calorimeter are in agreement. Table 5 contains all the values for different incidence angles, again offsets are not compatible with zero and the slopes are not in total agreement. This

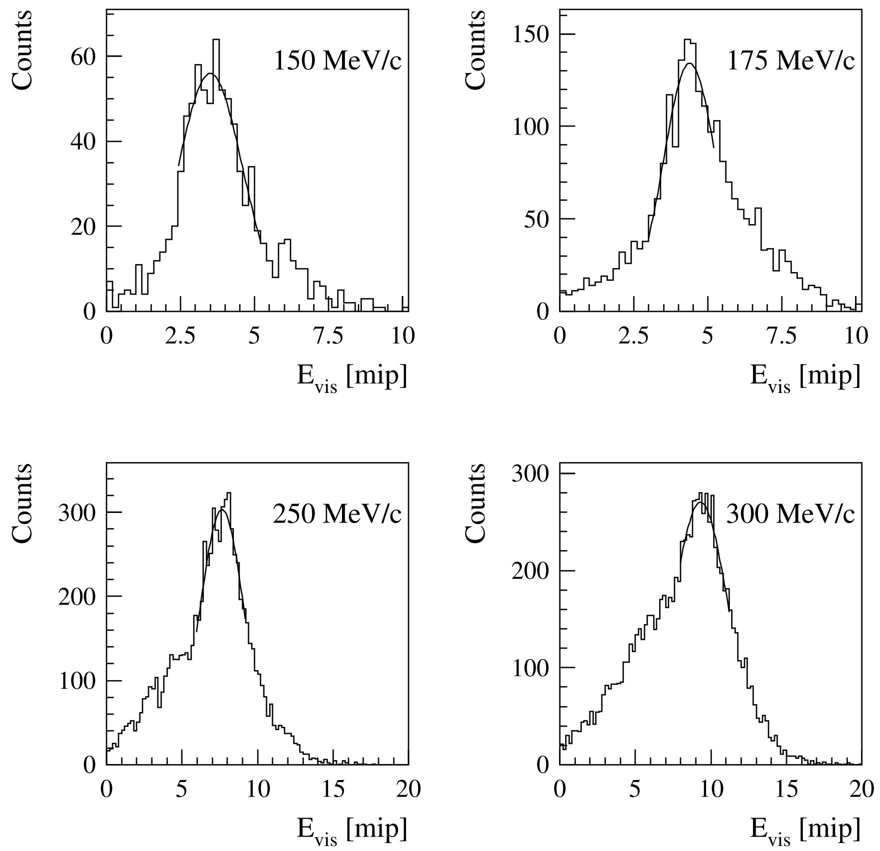

Figure 11: Energy spectra for pions at different momenta with superimposed Gauss fits.

Table 5: Energy response for pions at different incidence angles

φ	θ	s_π [mip/GeV]	offset [mip]
$0°$	$0°$	48.9 ± 0.8	0.764 ± 0.074
$20°$	$0°$	51.3 ± 1.7	0.470 ± 0.145
$0°$	$20°$	48.5 ± 2.1	0.710 ± 0.167
$0°$	$40°$	52.2 ± 2.3	0.406 ± 0.182

might be ascribed to the uncertainty in determining the peak value especially when there was a huge background due to nuclear reactions, cf. figure 11.

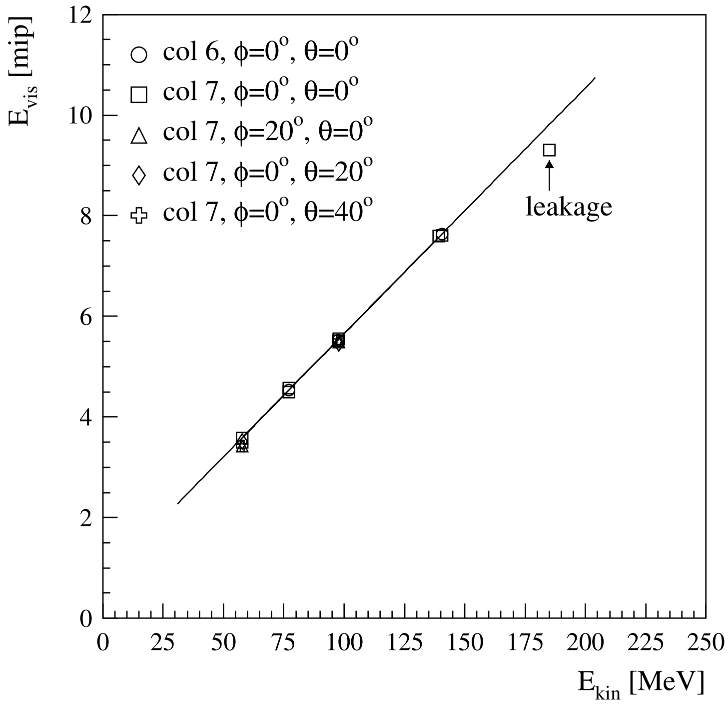

Figure 12: Energy response for pions, fit is for normal incidence only.

6.3 Energy Resolution for Electrons

To find the the energy resolution for electromagnetic showers we plotted the ratio between the sigma σ_E and the mean $< E_{vis} >$ values of the Gaussian energy distributions versus the kinetic energy of the electrons and found the well–known $\sqrt{E}$ behaviour:

$$\frac{\sigma_E}{< E_{vis} >} = \frac{4.96 \pm 0.01}{\sqrt{E\,[\mathrm{GeV}]}}\,\% \ .$$

No contribution of an energy independent term has been found thus confirming that the energy resolution is determined by photo electron and shower statistics.
Values for non–zero incidence angles can be found in table 6, they agree very well with the one found for $0°$.

z–Scan of Energy Resolution

Scans along the z–axis were performed at three different beam energies (125, 250 and 300 MeV), for 250 MeV the beam was impinging both on column 6 and 7. Results for the z–dependent energy resolution can be found in figure 14.
Only the contribution from the photoelectron statistics will be affected by different z–positions. Therefore we expect only a weak dependence of the energy resolution on the z–coordinate which is superimposed on the plots in figure 14. The curves are calculated with an "effective" attenuation length taken from the electron runs themselves

$$\lambda_{eff} = 340 \text{ cm},$$

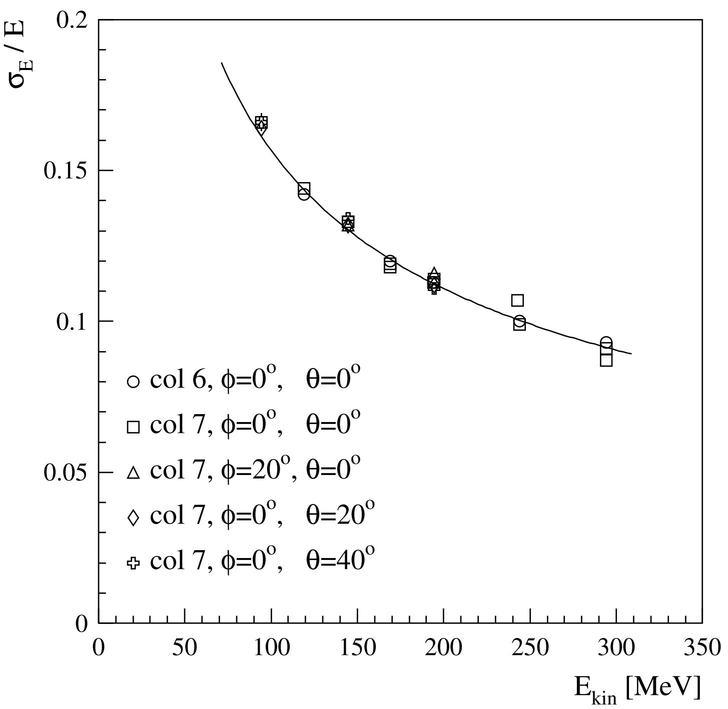

Figure 13: Energy resolution for electrons, fit is for normal incidence only.

Table 6: Angular dependence of the energy resolution

φ	θ	$\sigma_E / < E > \sqrt{E\,[\mathrm{GeV}]}$ in %
$0°$	$0°$	4.96 ± 0.01
$20°$	$0°$	5.09 ± 0.04
$0°$	$20°$	4.99 ± 0.03
$0°$	$40°$	4.98 ± 0.04

dominated by the properties of the Kuraray fibres in the first two planes.

6.4 Comparison with Prototype Results

When we compare the energy response from prototype results [Ant 94] with that from Module Zero it strikes that there seems to be a 6 % increase in the sampling fraction both for electromagnetic showers and muons stopping in the calorimeter. The reason for this is not yet understood, one could think of a different calorimeter composition or the smaller gaps between the readout cells.
Another idea is the existence of light cross talk between adjacent readout cells due to glue creeping between the light guides. Thus when performing the energy calibration one

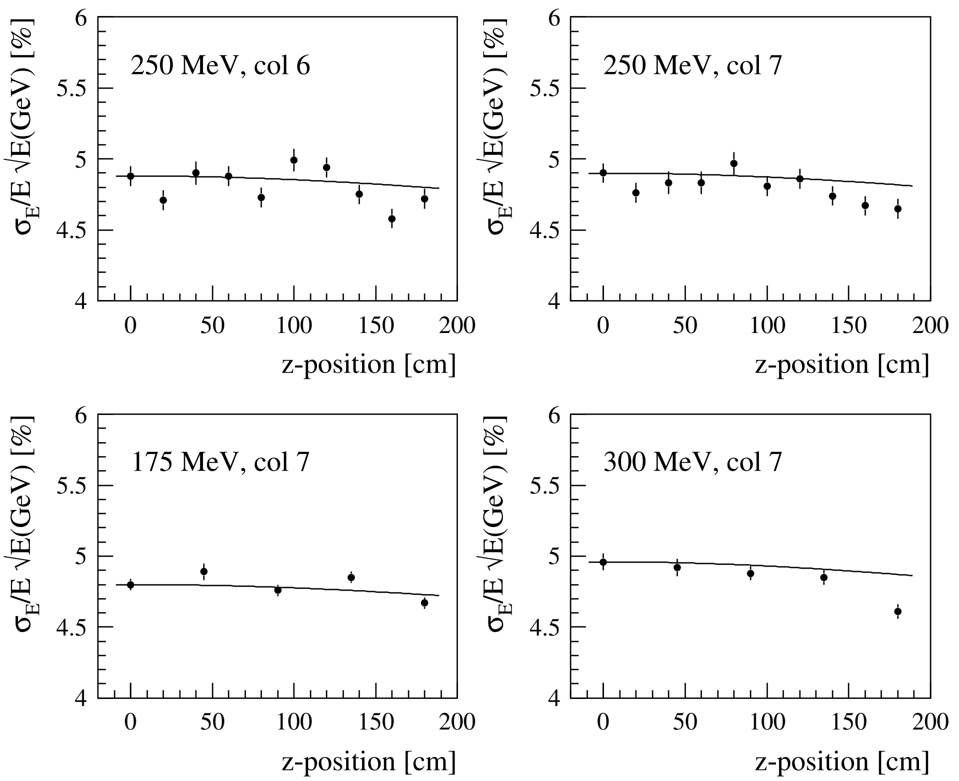

Figure 14: Energy resolution vs. z–position for electrons at normal incidence.

would discard light leaked to the neighbour cells and have therefore calibration constants that are too small. Instead when determining the energy of a shower, all contributing readout cells are added up and a higher energy response is faked. This is however still a hypothesis and needs further confirmation that could come from Cosmic Ray Stand data. The increased energy resolution instead can be attributed completely to the smaller number of photoelectrons produced. There are two parts determining the energy resolution: shower fluctuations and photoelectron statistics. The contribution due to photoelectron statistics p_{pe} can be estimated as

$$p_{pe} = 1/\sqrt{N_{pe}/\mathrm{GeV}}$$

and can be quadratically subtracted from the overall resolution value $p = \sigma_E / < E > \sqrt{E\,[\mathrm{GeV}]}$ to give the contribution due to shower fluctuations p_{sh}:

$$p_{sh}^2 = p^2 - p_{pe}^2 \ .$$

In first approximation we get both for prototype and Module Zero measurements the same shower contribution.
All relevant values are listed in table 7, values only valid for Pol.Hi.Tech fibres are put in parentheses.

Table 7: Comparison between prototype and Module Zero results

	Prototypes	Module 0	ratio
s_{em} [mip/GeV]	37.6 ± 0.3	40.0 ± 0.2	1.064
s_{μ} [mip/GeV]	46.8 ± 0.4	49.8 ± 1.2	1.064
s_{π} [mip/GeV]	47.9 ± 0.4	48.9 ± 0.8	1.021
e/μ ratio	0.803 ± 0.009	0.803 ± 0.020	—
$\sigma_E / < E > \sqrt{E}\,[\text{GeV}]$	(4.47 ± 0.020) %	(4.96 ± 0.01) %	—
N_{pe} per GeV	4 800	1 660 (1 075)	—
p_{sh}	4.2 %	4.3 % (4.0 %)	—

7 Time Resolution for Electrons

Discriminator Thresholds

The thresholds for the discriminators were rather high. Figure 15 shows typical curves for the TDC efficiencies vs. energy. If we define the threshold as the energy value where the efficiency is 0.5 we get values between 0.2 and 0.3 mip. This means that between 5 and 8 % of the visible energy could not been taken into account for the time information.

The usual variable used to express the event time is the energy averaged sum over all individual times

$$T_{sum} = \frac{1}{2} \sum_{i=1}^{n} \frac{(T_{A,i} + T_{B,i})\,(E_{A,i} + E_{B,i})}{(E_{A,i} + E_{B,i})} \ .$$

To get the time resolution we fit the distribution of T_{sum} with a Gaussian and take its sigma value σ'_{Tsum}. This value still contains the jitter of the start σ_{start} which has to be subtracted quadratically to get the real time resolution σ_{Tsum}

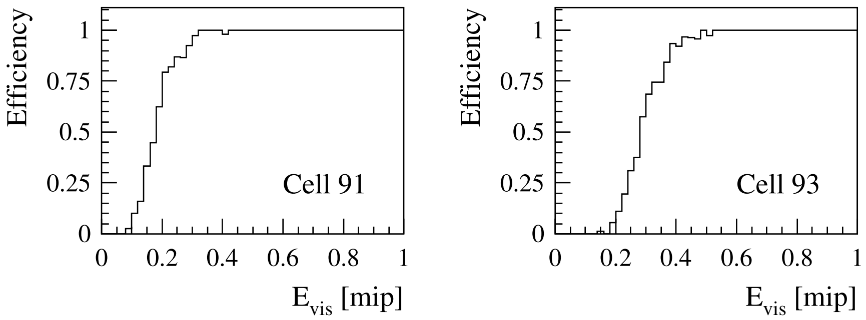

Figure 15: Typical curves for TDC efficiencies.

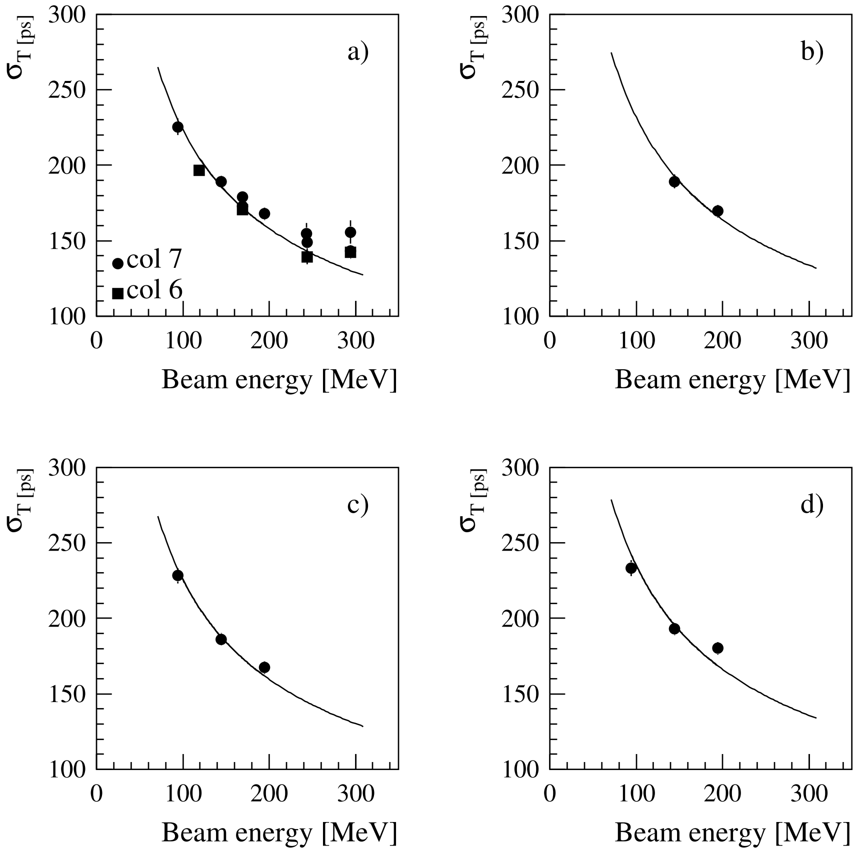

Figure 16: Time resolution for electrons:
a) $\varphi = 0°$, $\theta = 0°$, b) $\varphi = 20°$, $\theta = 0°$,
c) $\varphi = 0°$, $\theta = 20°$, d) $\varphi = 0°$, $\theta = 40°$.

$$\sigma_{Tsum} = \sqrt{\sigma'^{2}_{Tsum} - \sigma^{2}_{start}}\ .$$

Typical values for the start jitter were $\sigma_{start} = 180$ ps.
In figure 16 time resolution values are plotted vs. the kinetic energy for electromagnetic showers for various incidence angles. The curves can be described by a $1/\sqrt{E_{kin}}$ dependence. For 0° incidence angles we get

$$\sigma_{Tsum}(E_{kin}) = \frac{(71.7 \pm 1.0)\mathrm{ps}}{\sqrt{E\,[\mathrm{GeV}]}}\ .$$

For non–zero values of the incidence angles we get the slightly worse values that are listed in table 8.
Scaling from the prototype's result of $\sigma_T = 34$ ps$/\sqrt{E\,[\mathrm{GeV}]}$ [Ant 94] one would expect for the full size calorimeter module a time resolution of 58 ps for the Kuraray fibres and 72 ps for Pol.Hi.Tech fibres.
To see whether the rather large contribution of the start jitter influences the results we

have made a cross check by looking at the resolution of the time differences

$$T_{diff} = \frac{1}{2} \sum_{i=1}^{n} \frac{(T_{A,i} - T_{B,i})\,(E_{A,i} + E_{B,i})}{(E_{A,i} + E_{B,i})} \; .$$

Here the contribution from the start jitter cancels event by event but we have to take into account the size of the beam spot. It was defined by the cross section of the finger counters and is 1 cm in z–direction. Thus we have to subtract quadratically the corresponding resolution $\sigma_{t,beam}$

$$\sigma_{t,beam} = \frac{1}{\sqrt{12}}\ \mathrm{cm} \cdot {v_{eff}}^{-1} = 16.9\ \mathrm{ps} \tag{2}$$

from $\sigma'_{T\,diff}$ to end up with

$$\sigma_{T\,diff}(E_{kin}) = \frac{(72.0 \pm 0.3)\mathrm{ps}}{\sqrt{E\,[\mathrm{GeV}]}} \; ,$$

which is in perfect agreement with the resolution value from the time sum $\sigma_{T\,sum}$.

Table 8: Angular dependence of the time resolution

φ	θ	$\sigma_T \cdot \sqrt{E\,[\mathrm{GeV}]}$ in ps
$0°$	$0°$	71.7 ± 1.0
$20°$	$0°$	73.3 ± 1.3
$0°$	$20°$	71.4 ± 0.9
$0°$	$40°$	74.4 ± 1.0

7.1 z–Dependency of Time Resolution

As the time resolution is dominated by photoelectron statistics we should see a larger effect for the time resolution than for the energy resolution when moving from the centre of the module towards the edges. In figure 17 the results from z–scans at three different energies are presented, superimposed are the theoretically expected curves (again using an attenuation length of 340 cm), fixed at $z = 0$. Except for the 250 MeV scan where the beam was hitting column 7 the agreement is fairly good.

8 Z–coordinate

8.1 Reconstruction of the z–coordinate

Knowing the propagation velocity of the scintillation light in the fibres we can use the time difference from equation (3) to calculate the energy averaged z–coordinate z_{rec} of an event:

$$z_{rec} = \frac{1}{2} \sum_{i=1}^{n} \frac{(T_{A,i} - T_{B,i})\,(E_{A,i} + E_{B,i})}{(E_{A,i} + E_{B,i})}\, v_{eff} \tag{3}$$

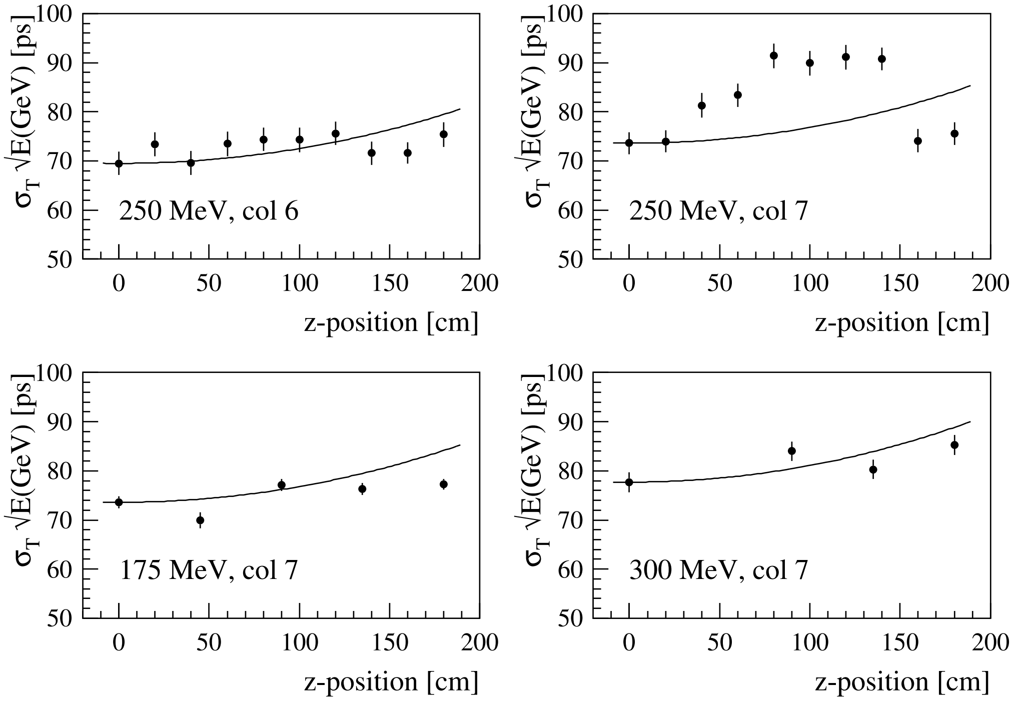

Figure 17: Time resolution vs. z–position for electrons at normal incidence.

where we have used the individual values of each plane for v_{eff}. In figure 18 we have plotted the difference between reconstructed and nominal z–position for three different energy ranges. There seems to be a systematic increase with an increasing distance from the centre. The reason could be the problems with the TDC calibration. Nevertheless the largest deviation is 1 cm.

8.2 Resolution in z

The spatial resolution in the z–direction σ_z we get when from the sigma values of the Gaussian fit of the z_{rec} distributions. Again we have to subtract quadratically the sigma of the beam spot, cf. equation (2), $\sigma_{z,beam} = 0.29$ cm. In figure 19 we have displayed σ_z depending on the kinetic energy for electrons at normal incidence. A fit gives the following energy dependence:

$$\sigma_z(E_{kin}) = \frac{(1.24 \pm 0.1)\mathrm{cm}}{\sqrt{E\,[\mathrm{GeV}]}} \ .$$

In figure 20 values for the z–resolution are given for different z–scans. A comparison with figure 17 shows that the shape of the is roughly the same, thus we are dealing with the same systematics both for time sums and differences.

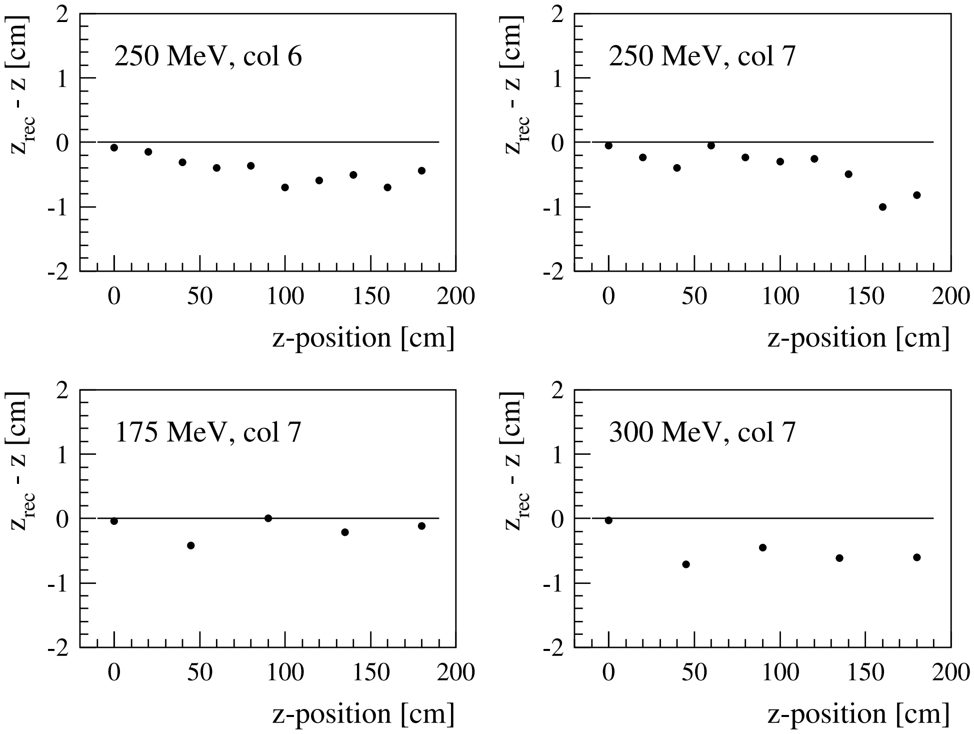

Figure 18: Difference between reconstructed and nominal z–position vs. nominal z–position for electrons at normal incidence.

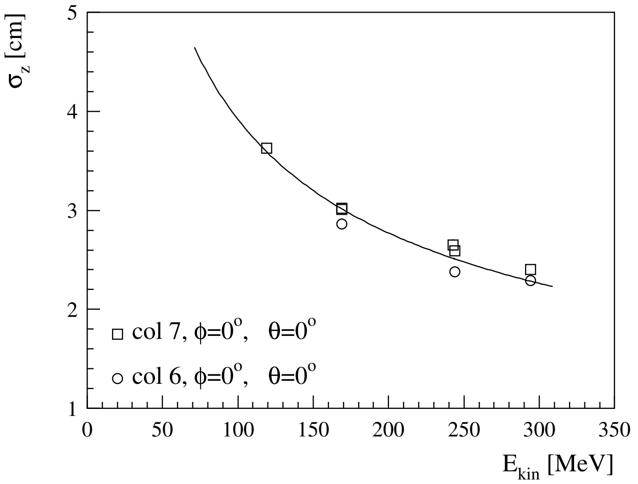

Figure 19: z–resolution vs. kinetic energy for electrons at normal incidence.

9 Summary

The energy and time resolution properties of the *barrel* Module Zero are in agreement with those from former prototypes when we take into account its bigger length and the 45 % smaller quantum efficiency of the mesh phototubes which both result in a smaller number of photoelectrons. We can summarize the results achieved in the previous sections as follows:

- Fibre characteristics of Kuraray, values for Pol.hi.Tech in parentheses:
  Number of photolectrons per GeV: 1 660 (1 075)
  Attenuation length: $\lambda = 360$ cm (230 cm)
  Light propagation velocity: $v_{eff} = 17.1$ cm/ns (17.4 cm/ns)

- Sampling fraction for electromagnetic showers:

$$f_{em} = (13.0 \pm 0.1)\,\%$$

  not depending on incidence angles.

- Sampling fraction for muons and pions stopping in the calorimeter:

$$f_{\mu} = (16.1 \pm 0.4)\,\% \text{ at normal incidence}$$

- e/μ–ratio:

$$\frac{f_{em}}{f_{\mu}} = 0.803 \pm 0.09$$

- Energy resolution for electromagnetic showers at normal incidence:

$$\frac{\sigma_E}{< E_{vis} >} = \frac{4.96 \pm 0.01}{\sqrt{E\,[\mathrm{GeV}]}}\,\% \;.$$

  No dependence on incidence angle found, dependence on z–position in agreement with photoelectron statistics.

- Time resolution for electromagnetic showers:

$$\sigma_T(E_{kin}) = \frac{(71.7 \pm 1.0)\mathrm{ps}}{\sqrt{E\,[\mathrm{GeV}]}} \text{ at normal incidence,}$$

  getting slightly worse with increasing polar or azimuthal angle (up to 4 % at $\theta = 40°$).
  Dependence on z–coordinate can be attributed completely to photoelectron statistics.

- z–reconstruction properties are satisfactory.

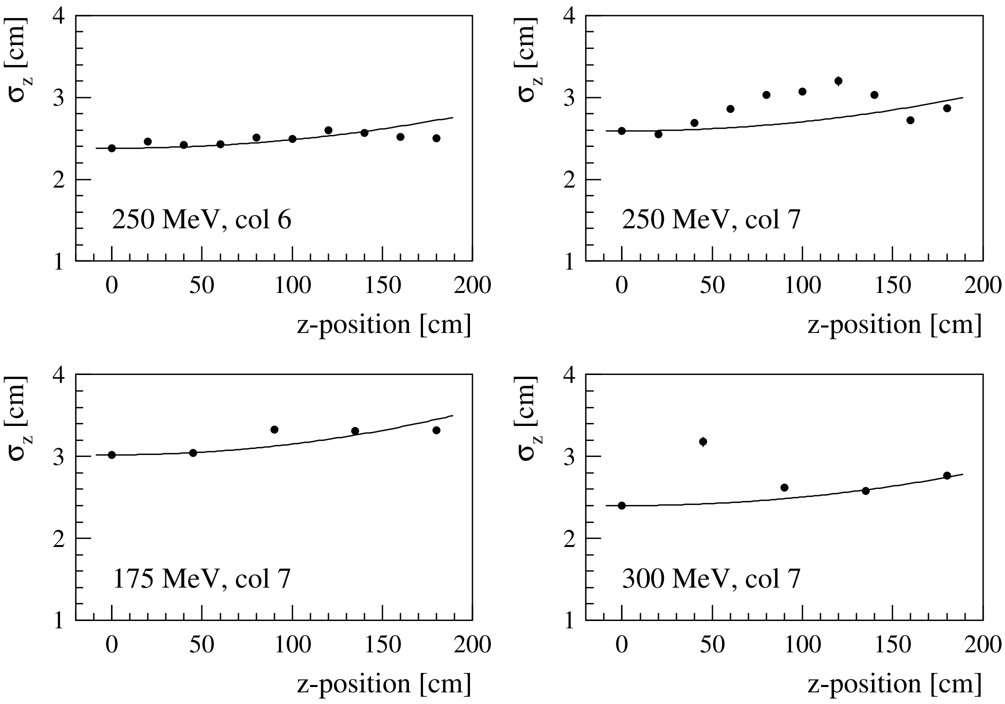

Figure 20: z–resolution vs. z–position for electrons at normal incidence.

References

[And 94] A. Andryakov *et al.*, *KLOE Metric*, KLOE Note 115 (1994)

[Ant 94] A. Antonelli *et al.*, *Construction and Performance of the Lead–Scintillating Fiber Calorimeter Prototypes for the KLOE Calorimeter*, LNF report LNF–94/049 (1994)

[CDF 93] M. Shapiro *et al.*, *A beginner's guide to ANALYSIS_CONTROL and BUILD_JOB*, CDF Note 384 (1993)

[Gio 94] S. Giovanella, private communication

[Kee 94] L. Keeble *et al.*, *Experimental Comparison of Timing Properties of Linear-Focussed and Mesh Photomultiplier tubes*, KLOE Note 90 (1994)

[Mur 94] F. Murtas, private communication

[Pel 94] F. Pelucchi *KLOE Database server for test beam*, KLOE Note 123 (1994)

[Wöl 95] S. Wölfle, *Calibration Routines for the 1994 Calorimeter Test Beam*, KLOE Note 135 (1995)

Acknowledgements

I would like to acknowledge the efforts of all those who have contributed to the 1994 test beam at PSI. In particular I would like to thank F. Donno and F. Pelucchi for creating a very organized software environment both for `ANALYSIS_CONTROL` and the databases, S. Giovanella, R. Haydar, L. Keeble and S. Miscetti for their participation in writing `A_C` modules and F. Murtas for providing his TDC calibration values. Special thanks go to S. Miscetti also for many discussions, his help and support.